Temperature dependence of fluid transport in nanopores

Baoxing Xu,[1] Binglei Wang,[2] Taehyo Park,[3] Yu Qiao,[4,5] Qulan Zhou,[6] and Xi Chen[1,3,7,a)]
[1]*Columbia Nanomechanics Research Center, Department of Earth and Environmental Engineering, Columbia University, New York, New York 10027, USA*
[2]*Department of Engineering Mechanics, Shandong University, Jinan, Shandong 250061, China*
[3]*Department of Civil and Environmental Engineering, Hanyang University, Seoul 133-791, South Korea*
[4]*Program of Materials Science and Engineering, University of California – San Diego, La Jolla, California 92093, USA*
[5]*Department of Structural Engineering, University of California – San Diego, La Jolla, California 92093-0085, USA*
[6]*State Key Lab of Multiphase Flow, Xi'an Jiaotong University, Xi'an 710049, China*
[7]*International Center for Applied Mechanics, SV Laboratory, and School of Aerospace, Xi'an Jiaotong University, Xi'an 710049, China*

(Received 22 February 2012; accepted 21 April 2012; published online 8 May 2012)

Understanding the temperature-dependent nanofluidic transport behavior is critical for developing thermomechanical nanodevices. By using non-equilibrium molecular dynamics simulations, the thermally responsive transport resistance of liquids in model carbon nanotubes is explored as a function of the nanopore size, the transport rate, and the liquid properties. Both the effective shear stress and the nominal viscosity decrease with the increase of temperature, and the temperature effect is coupled with other non-thermal factors. The molecular-level mechanisms are revealed through the study of the radial density profile and hydrogen bonding of confined liquid molecules. The findings are verified qualitatively with an experiment on nanoporous carbon. © *2012 American Institute of Physics*. [http://dx.doi.org/10.1063/1.4712034]

INTRODUCTION

When liquid molecules are confined in a nanoenvironment, owing to the unique interaction characteristics with the nanopore wall, the nanofluidic behaviors often cannot be directly described by conventional continuum fluid mechanics theories.[1–3] Among these unique phenomena, the transport behavior has attracted significant interest,[4–7] which may facilitate the development of nanodevices with high efficiency. For water flow through carbon nanotubes (CNTs), using molecular dynamics (MD) simulations, Hummer *et al.*[8] discovered the ultra-fast transport of water through small CNTs. Majumder *et al.*[9] fabricated an array of aligned CNTs with diameter of 6.0 nm, and confirmed that the transport rate was up to 4–5 orders of magnitude higher than that predicted from conventional fluid-flow theory. Similar findings were reported by Holt *et al.*[10] for CNTs with diameter less than 2.0 nm. Recent MD simulations also confirmed that the water molecule transport behavior in CNT is strongly size dependent and rate dependent.[11]

The enhanced transport rate in nanopores may be attributed to the atomic smoothness of nanopores and their hydrophobicity. The former leads to a small friction[12–14] and the later induces a depletion region[8,9,13] at the liquid-solid interface. Joseph and Aluru[15] examined both the effects by studying water transport through a CNT of diameter 1.6 nm, and showed that the hydrophobic interaction between water molecules and nanopore wall has more enhancement on the transport rate in comparison to the wall smoothness. Several strategies of adjusting the hydrophobicity have been put forward, such as applying electric fields[16–18] or employing electrolyte liquids.[19,20] It is well known that the viscosity of water decreases at elevated temperature,[21,22] and the hydrophobicity at the nanoscale also depends on temperature[23] (which has been used to pump nanofluids[24–26]). To the authors' knowledge, however, the temperature-dependent transport behavior of nanofluids still remains unexplored.

Since the confined nanofluidic transport is a typical non-equilibrium process,[27,28] in the present study, we employ the non-equilibrium molecular dynamics (NEMD) (Refs. 11, 20, and 27) simulations and experiments to investigate the temperature-dependent characteristics of nanofluidic transport. For a reference system of water transport in a model CNT, the thermal dependence of the effective shear stress and nominal viscosity are explored as the CNT size and flow velocity are varied. The thermal effect of electrolyte liquid transport is also studied and the behaviors are compared with that of pure water. The underlying molecular mechanism is elucidated by the temperature dependence of radial density distribution and hydrogen bonding. A parallel experiment on a nanoporous carbon/water system is carried out to qualitatively verify the NEMD simulation findings.

COMPUTATIONAL MODEL

Simulation model and force field

A segment of CNT is employed to model a smooth nanopore structure (Figure 1). The axial length of the CNT, L, is chosen to be $8R$, where R is the radius of the CNT. The

a)Author to whom correspondence should be addressed. Electronic mail: xichen@columbia.edu.

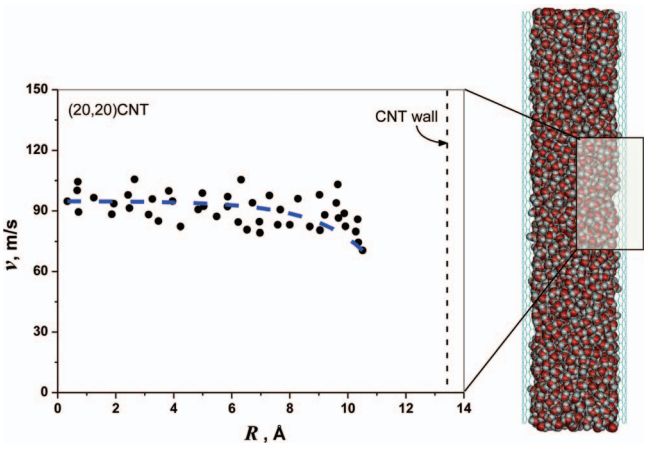

FIG. 1. The average axial velocity distribution (in the radial direction) of water molecules inside a (20,20) CNT at 300 K. The diameter of the (20,20) CNT is 2.71 nm.

density of water molecules inside the occupied volume of CNT is set to be close to that of bulk water, $\rho_o = 998.0\ \text{kg/m}^3$, at 300 K and 1 atm. Periodical boundary condition is imposed in the axial direction of the computational cell so as to mimic an infinite long pore and minimizing the entrance and exit effects on the transport behavior.[12,20,28] The periodic length of $8R$ has been verified to be long enough for robust data collection.

The simulation is performed using large-scale atomic/molecular massively parallel simulator (LAMMPS).[29] Since the effect of CNT flexibility is relatively small,[30] in the present study the nanopore wall is assumed rigid. The water molecules are modeled by the extended simple point charge potential,[31] and constrained by the SHAKE algorithm. The 12-6 pairwise Lennard-Jones (L-J) potential and Coulomb interaction, $U(r_{ij}) = 4\varepsilon_{ij}[(\sigma_{ij}/r)^{12} - (\sigma_{ij}/r)^6] + q_i q_j/(4\pi\varepsilon_0 r)$, are used to model the water-water interaction and carbon-water interaction, where r denotes the distance between atoms i and j, ε_{ij} and σ_{ij} are the energy and length parameters for a i-j pair atom, respectively, q_i and q_j are the electric charge counterpart, and ε_0 is the permittivity of vacuum. When other electrolyte solutions are employed, this governing potential equation is also used to describe the interaction between ions and atoms. The cross interactions are obtained by using the Lorentz-Berthelot mixing rules, $\varepsilon_{ij} = \sqrt{\varepsilon_{ii}\varepsilon_{jj}}$, and $\sigma_{ij} = (\sigma_{ii} + \sigma_{jj})/2$. The relevant L-J parameters are taken from Refs. 32 and 33 and listed in Table I. These parameters have been confirmed to reproduce the experimental information such as contact angle of water droplet on a graphite surface[34] and the binding energies of ion-water interactions.[33] All L-J interactions are truncated at a cut-off distance of 1.0 nm to calculate the short-range van der Waals forces,[35] and the particle-particle particle-mesh solver with a root mean-square accuracy of 10^{-4} is applied to account for the truncation of the long-range electrostatic force.[36] In the present study, the temperature varies between 300 and 360 K, and within such a moderate range, it is generally assumed that the force field parameters can be kept the same throughout simulation.[37,38] Besides, within this temperature range, there is no phase transition for the employed CNTs (with the diameter between 0.81 and 2.71 nm) under the pressure of 1 atm.[39,40]

TABLE I. The 12-6 L-J potential parameters used in the MD simulation.[32,33]

Atom/ion	ε (kcal/Å)	σ (Å)	q(e)
C	0.29622	3.215	0
H	0	0	+0.4238
O	0.6502	3.166	− 0.8476
Na^+	0.4184	2.586	+1
K^+	0.4184	3.334	+1
Cl^-	0.4184	4.404	− 1

Simulation implementation and procedure

Several methods have been developed to simulate nanofluidic behaviors using NEMD techniques, such as gravity-driven flow,[12,15,41] dual control volume grand canonical molecular dynamics,[42] and fluidized piston-driven flow,[43] among others. The gravity-driven flow is particularly attractive because of its computational simplicity, and it also allows us to focus on the properties of the fluid. In this approach, a homogeneous stable flow is generated by applying an analog of gravity force to each molecule in the flow direction. When a steady flow with a desired flow rate is reached, in order to better measure the flow resistance (in comparison with the thermal noise), the applied gravity force is removed to allow the molecules to flow and decelerate freely.

The simulation procedure consists of two steps: In the first step, after initialization at a desired temperature, the *NVT* ensemble is employed for 0.1 ns to equilibrate the system, and then a constant gravity acceleration is applied on each water molecule along the axial direction of the CNT so as to initiate a uniform flow inside the nanotube. During this stage, the temperature is maintained by using a Nose/Hoover thermostat with a time constant of 0.2 ps, and it is only applied to the liquid phase since the CNT is assumed to be rigid. To avoid artificial heating caused by the imposed axial displacements, the mean axial velocity of the liquid mass center is subtracted from the axial component of the velocity of each liquid molecule during the calculation of temperature. After a desired transport velocity, $\bar{v}$, is reached, in the second step, the applied acceleration is removed and the molecules are allowed to flow freely and only subjected to the transport "friction" resistance from carbon wall. Afterwards, the NVE ensemble is employed to monitor the velocity and deduce fluidic characteristics (see below).

SIMULATION RESULTS AND DISCUSSION

Fundamental transport behaviors upon different temperatures

We first examine the velocity profile of water molecules inside the CNT. For a representative (20,20) CNT/water system, the average axial velocity of water molecules across the CNT section (at the temperature of $T = 300$ K) is plotted in

Figure 1. The overall velocity profile is plug like, featuring almost uniform velocity except the reduction near the pore wall, consistent with the literature.[11,43]

After a desired $\bar{v}$ is reached, the liquid molecules are allowed to freely decelerate. The average flow rate is recorded to identify an initial linear decelerating window (about 0.1 ns), during which its magnitude drops by a small percentage; at the same time, the system temperature is closely monitored to make sure that there is no sudden rise in system temperature. Upon the deduction of the average deceleration, $\bar{a}$, the effective shear stress at the liquid-solid interface can be defined as $\tau|_{r=R} = \tau = \sum m_i \bar{a}/(2\pi R' L)$,[11] where $\sum m_i$ is the total mass of all water molecules inside the tube, and R' is the accessible radius of liquid molecules occupied in the tube.[20] As an "overall" measure of the transport resistance of nanofluidic flow, the direction of τ is opposite to the axial flow direction. During the computation of $\bar{a}$, the system temperature is closely monitored to make sure that there is no sudden rise in system temperature.

In a nanofluidic system, the most dominate characteristic is the interaction between solid wall and liquid molecules immediately near it, and the conventional Newton's law of viscosity may be invalid for highly inhomogeneous nanofluid.[28,44] The effective shear stress τ, whose majority is exerted by the carbon wall to water molecules, is perhaps a more reliable measure of the transport resistance.[11,20] Based on the obtained the shear stress τ, we further define a nominal viscosity, $\tilde{\eta} = \tau R/(4\bar{v})$,[11,45] a quantity that has the same dimension as conventional viscosity. It is largely based on the solid-liquid interaction and reflects the "easiness" of water transporting through a nanochannel. Although the present nominal viscosity is different from the conventional bulk liquid viscosity, it is still useful for revealing the size, rate, and temperature effects of nanofluids.[11,20] In what follows, these two parameters (τ and $\tilde{\eta}$) are employed to study the temperature-dependent transport behavior, and the primary focus is given to τ.

At $\bar{v} = 100$ m/s, the effective shear stress τ and nominal viscosity $\tilde{\eta}$ for water molecules transporting in a (20,20) CNT are obtained at different temperatures, shown as solid square curves in Figure 2, and both of them decrease with the increase of T. The error bar arises from the small uncertainty of determining the deceleration. When Figure 2 is repotted in a semi-log coordinate system (not shown here), it can be verified that $\tilde{\eta}$ varies as exp (1/T), a characteristic that is somewhat similar to the viscosity of bulk water,[21,22] although it is reminded that the nominal $\tilde{\eta}$ for nanofluidic transport is largely caused by the liquid-solid wall interaction, yet the viscosity of bulk fluid is dominated by the interaction among liquid molecules.

In addition, the pore size effect is coupled with the temperature effect. By studying three other CNTs with chirality (16, 16), (10, 10), and (6, 6) (whose diameters are 2.17, 1.36, and 0.81 nm, respectively), it is found that the values of τ and $\tilde{\eta}$ in smaller tubes are lower than their counterparts in larger tubes. That is, smaller CNTs may benefit higher water flow rate, consistent with Refs. 8 and 10. More importantly, in a smaller tube, as the temperature increases, there is a faster decreasing trend of τ and $\tilde{\eta}$ (than that in a larger tube), indicating that the transport resistance is more sensitive to temperature variation in a smaller tube. This phenomenon is consistent with the increasing role of liquid-solid interaction on nanofluidic transport with the decrease of CNT size.[11,46]

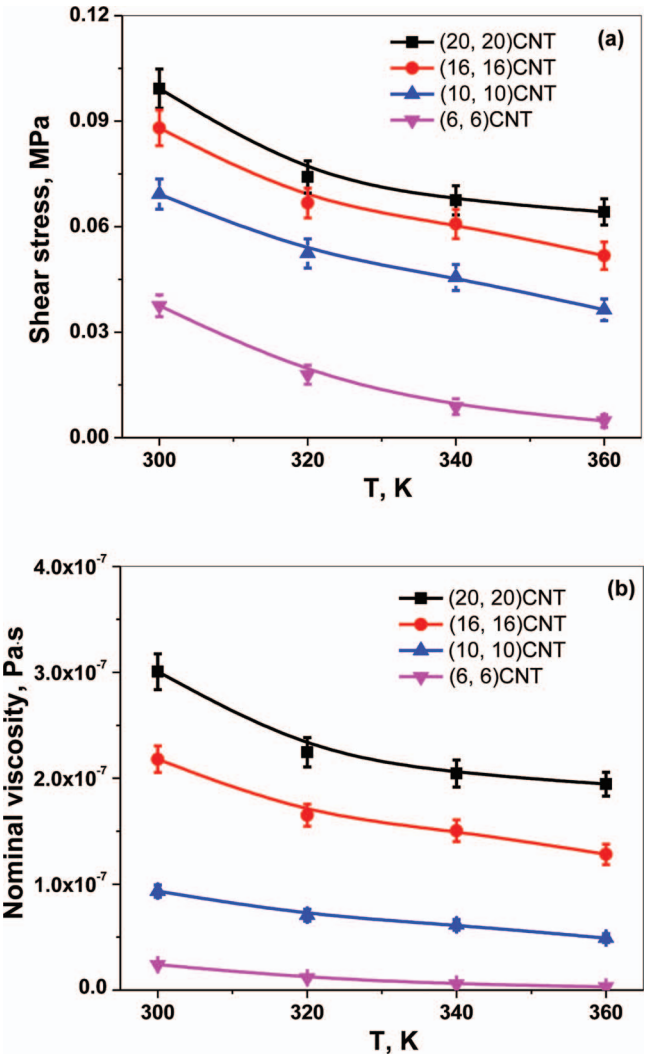

FIG. 2. Effect of temperature on the (a) effective shear stress and (b) nominal viscosity for different CNT sizes at the transport rate of 100 m/s.

The influence of transport rate is also coupled with the thermal effect. In Figure 3, a (20,20) CNT and a (6,6) CNT are chosen as representatives of a large and small tube, respectively, and $\bar{v}$ varies as 100 m/s, 150 m/s, and 200 m/s. In general, the transport resistance increases with the increase of $\bar{v}$, while the nominal viscosity, $\tilde{\eta}$, decreases with the increase of flow rate. At a higher transport rate, since there is no sufficient time for the molecules to fully adjust their positions to minimize the system energy, the overall van der Waals repulsion is more prominent, leading to a higher shear stress.[11] Again, if the CNT diameter is smaller, the temperature sensitivity of the effective shear stress and nominal viscosity is more prominent, which may benefit relevant applications in the design of thermomechanical nanofluidic devices.

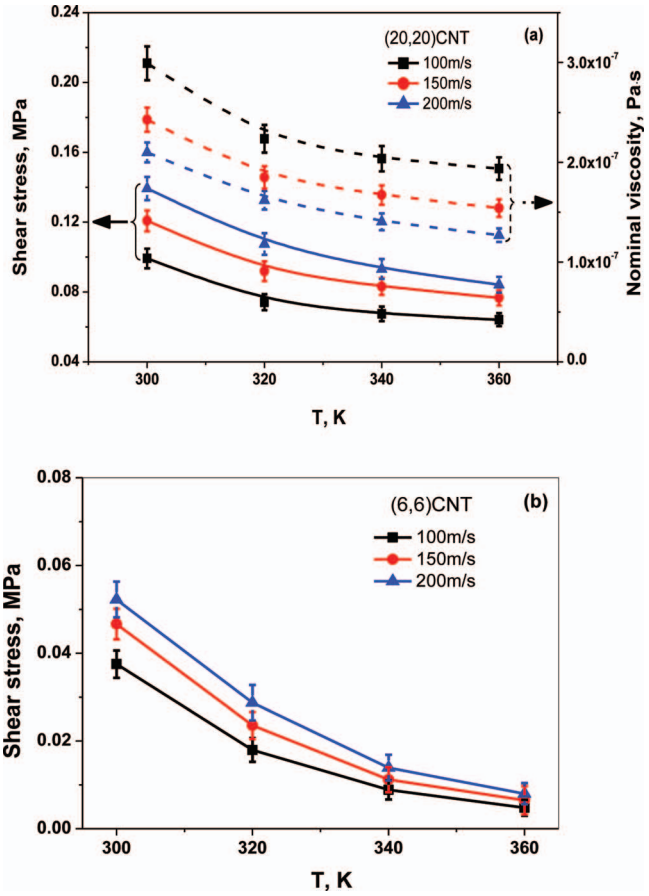

FIG. 3. Effect of temperature on the effective shear stress (solid curves) and nominal viscosity (dash curves) on (a) (20,20) CNT/water system and (b) (6,6) CNT/water system at different transport rates.

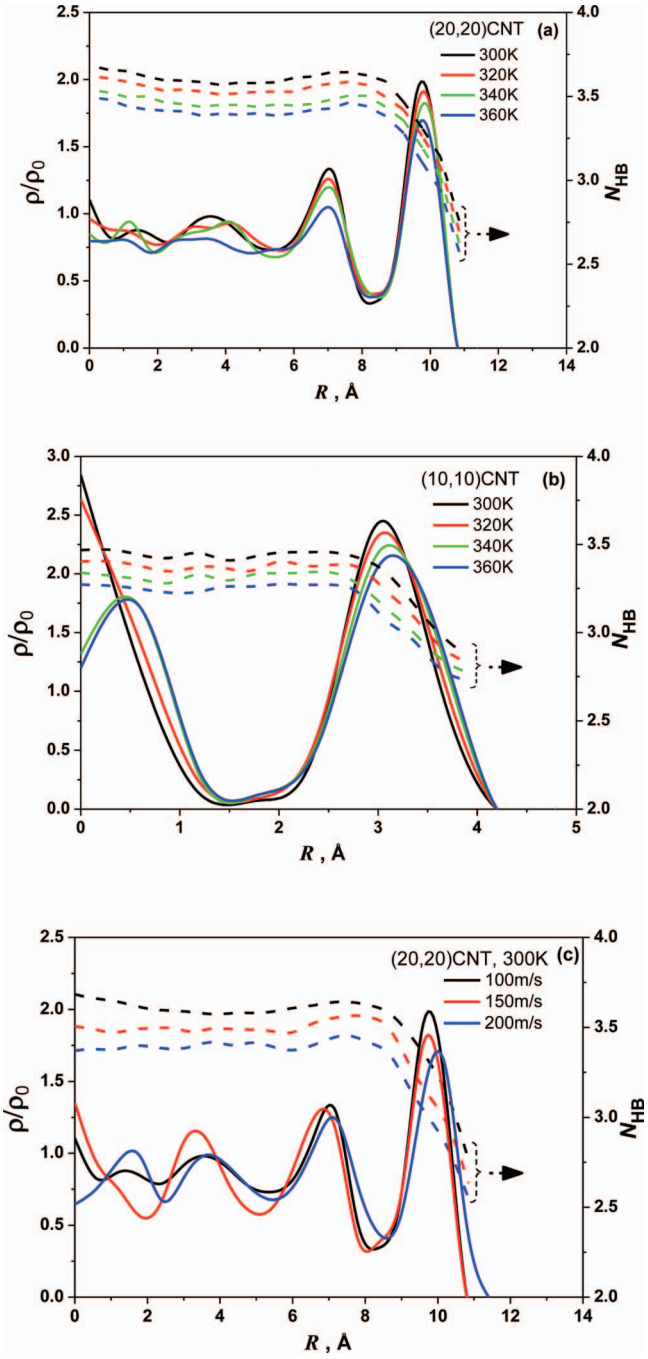

FIG. 4. Normalized radial density profile, ρ/ρ_0 (solid curves), and the number of hydrogen bond per water molecule, N_{HB} (dash curves), in the (a) (20,20) CNT/water system and (b) (6,6) CNT/water system at different temperatures, all at the same transport rate of 100 m/s; and (c) (20,20) CNT/water system at different transport rates and the same temperature of 300 K.

Molecular mechanism of temperature effect coupling with size and transport rate effects

Nanofluidic transport behavior is underpinned by the liquid-solid wall interaction. In essence, the transport behavior reflects the non-bond force imposed by the solid wall on liquid molecules, and a stronger van der Waals' constraint will lead to a larger effective shear stress. The radial density profile and hydrogen bonding may help to reveal the configuration and structural distribution of confined water molecules inside a CNT. Both of them are employed to reveal molecular mechanism of the temperature-dependent transport behavior coupling with pore size effect and transport rate effect, and explored below.

Figures 4(a) and 4(b) give the effect of temperature on the radial density profile in (20, 20) CNT and (10,10) CNT/water systems at the transport rate of 100 m/s, respectively. The fluctuations indicate the annular layered structures of water molecules inside CNTs.[11,47] The maximum density near the wall is usually referred as the first solvation shell (FSS), whose spacing to the wall is the equilibrium distance. With the increase of temperature, both the amplitude of FSS and equilibrium distance decrease, which imply a weaker solid wall-water interaction. Moreover, under such a circumstance, the radial confinement effect imposed on the water molecules is less severe, and thus the axial component of the velocity of water molecules is relatively more prominent, leading to smaller transport resistance and effective shear stress. When the diameter of CNT decreases (Figure 4(b)), the effect of temperature on the variations of both the FSS amplitude and the equilibrium distance becomes more prominent, which qualitatively echoes with the coupling between size effect and temperature effect (i.e., the transport resistance in smaller tubes is more thermally responsive).

Figure 4 gives the variation of the number of the averaged hydrogen bond per water molecule, N_{HB}, which is calculated by dividing the total number of hydrogen bonds

by the total number of water molecules in each annual layer along the radial direction. The calculation of N_{HB} is based on geometry,[48] where two water molecules are assumed to be hydrogen-bonded only if (a) the oxygen-oxygen distance is smaller than 3.5 Å and simultaneously (b) the bond angle between the oxygen-oxygen direction and one of the oxygen-hydrogen directions is less than 30°. From Figure 4, N_{HB} arrives maximum at the center of CNT, close to that calculated for bulk water (3.78), and decreases away from the center. Overall, at a higher temperature, or higher transport velocity, the value of N_{HB} is smaller, which leads to a lower transport resistance, consistent with simulations. The drop of N_{HB} near the water-CNT interface indicates the local depletion of hydrogen bond and a weakened water network structure near the solid wall, consistent with previous studies.[8,15,49] In addition, a larger CNT shows a more significant drop of N_{HB} near the water-CNT interface, leading to larger transport resistance and larger effective shear stress, which also agree with above simulations.

Water transport vs. electrolyte solution transport

The preceding study on the water/CNT system shows that the effective shear stress and nominal viscosity depend primarily on the solid-liquid interfacial interaction. When the liquid phase changes, the transport behavior is expected to vary,[7,20,50,51] and in this section, we focus on the thermal effect of electrolyte transport in CNT. The NaCl and KCl solutions are chosen as substitutes of the water liquid phase, whose concentration is maintained at 2.0 mol/l. Following the same simulation procedure above, taking a (20,20) CNT and a (6,6) CNT as representatives of a large and small pore, respectively, the variations of the effective shear stress and nominal viscosity with temperature (at $\bar{v} = 100$ m/s) are given in Figures 5(a) and 5(b), respectively. Both of them decrease with the increase of temperature, similar with those of water/CNT system, but are larger in respective amplitudes. Besides, they also show intriguing ion size dependence: a larger ionic size ($K^+ > Na^+$) leads to a higher effective shear stress and nominal viscosity because of a stronger interaction between a larger ion, water, and CNT. With the decrease of CNT size (Figure 5(b)), the deviation of the effective shear stress between electrolyte solution and pure water system increases.

The corresponding radial density profile of water molecules and N_{HB} is plotted in Figure 5(c). Both the amplitude of FSS and the equilibrium distance are larger in the system with electrolyte solution (compare with that of pure water phase). When electrolyte solutions are employed, owing to the electrostatic interaction of ions with water molecules, the water molecules tend to become more cohesive (which can also be validated from the increase of N_{HB} in the CNT/electrolyte solution system), leading to the increase of amplitude of FSS and equilibrium distance, with more prominent radial confinement effect, and thus a higher effective shear stress.

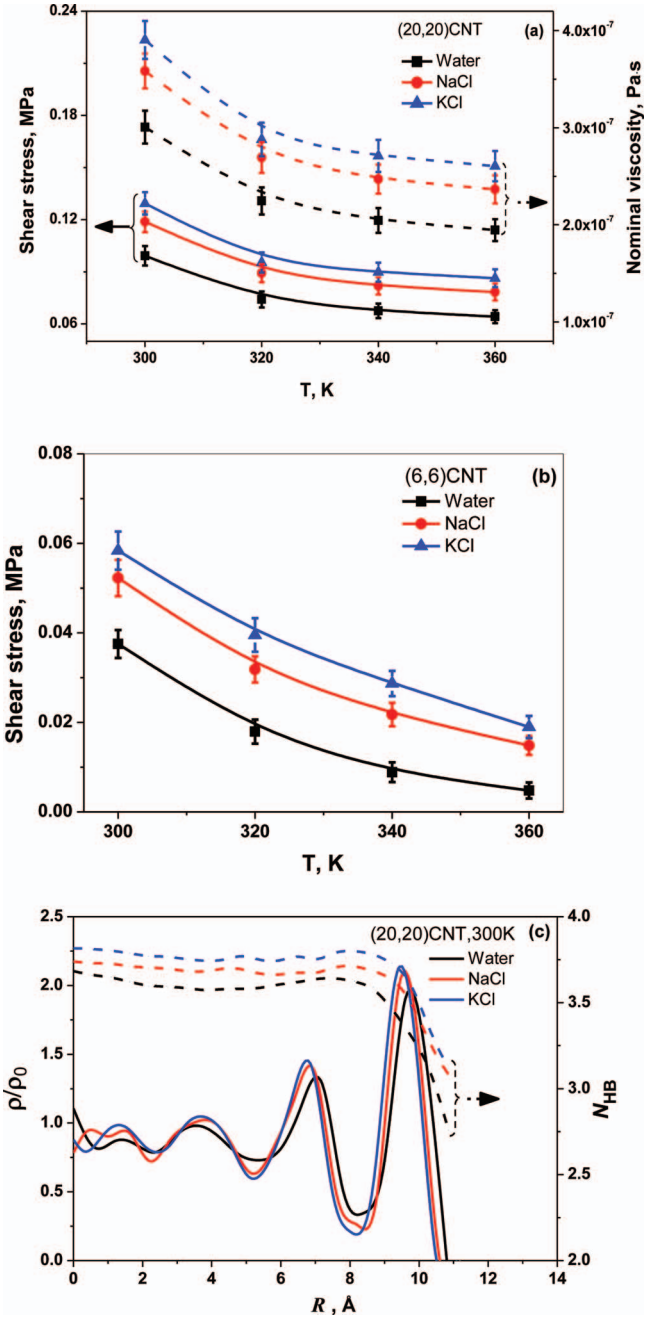

FIG. 5. Temperature-dependent transport behavior in CNT/electrolyte solution system. Effect of temperature on the effective shear stress (solid curves) and nominal viscosity (dash curves) in (a) (20,20) CNT/electrolyte solution system, (b) (6,6) CNT/electrolyte solution system, (c) the normalized radial density profile, ρ/ρ_0 (solid curves), and the number of hydrogen bond per molecule, N_{HB} (dash curves), at 300 K. The transport velocity is 100 m/s.

COMPARISON WITH EXPERIMENTAL DATA

A pressure-induced infiltration (PII) experiment was carried out on a nanoporous carbon, and its data are qualitatively compared with the above NEMD simulation results. The material under investigation was Cabot BP-2000 nanoporous carbon, with the smallest nanopore radius of about 1.0 nm and the largest nanopores around 100 nm. Through a Brunauer-Emmett-Teller (BET) analysis, it was measured that the specific nanopore surface area was 1400 m^2/g. The as-received material was in powder form, with the particle size of about 50 μm. For the nanoporous carbon materials, the inner surface of nanopores was hydrophilic as received. If the untreated nanoporous carbon was immersed into the liquid

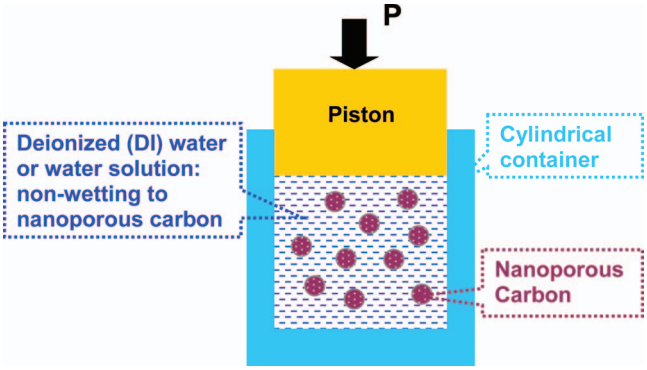

FIG. 6. Schematic of experimental setup. Due to the non-wetting of liquid phase to nanopore carbon, the liquid will not intrude into nanopores. As the external pressure, P, increases, the solid-liquid interfacial capillary force is overcome and the liquid starts to infiltrate into nanopore, leading to the decrease of system volume. The continuous transport of liquid inside nanopore can be employed to study the interfacial property between the solid wall and liquid phase.

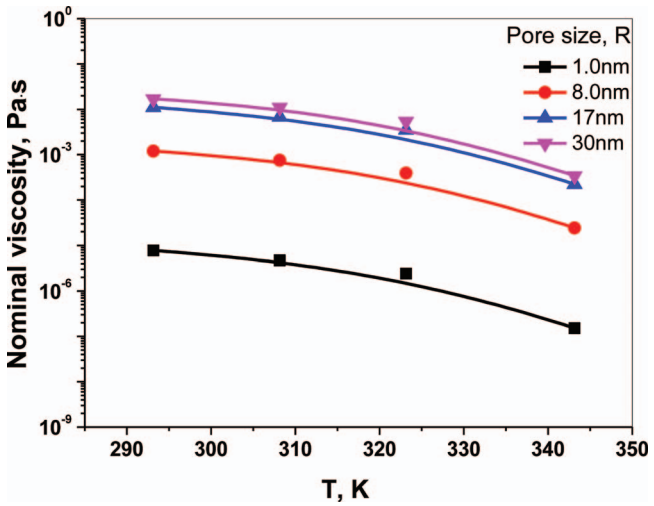

FIG. 7. Calculations of the nominal viscosity with temperature and pore size from a pressure-induced infiltration (PII) experiment on a nanoporous carbon/deionized water system.

phase (deionized water), the water molecules would spontaneously enter the nanopores, which makes it extremely difficult to deduce the nominal viscosity. Therefore, prior to the PII experiment, the nanoporous carbon was treated by silyl groups to modify the properties of the inner pore surfaces and achieve hydrophobicity, the details of which has been given elsewhere.[45]

In a stainless steel cylinder, 0.3 g of the surface modified nanoporous carbon and 5.5 g of deionized water were sealed by two stainless steel pistons. The pistons were equipped by reinforced o-rings. The schematic of the experimental setup is shown in Figure 6. The cross-sectional area of the piston was $A_p = 286\ \text{mm}^2$. The temperature of the testing cell was kept at 293 K, 308 K, 328 K, or 348 K by using an Aldrich DigiTrol II Z28 water bath.

By using a type 5580 Instron machine, the upper piston was continuously intruded into the cylinder at a constant rate and an external pressure was applied on the water liquid phase. The piston displacement rate, v_p, was 5 mm/min. The PII process starts from the largest nanopores, and as the pressure increased, more and more smaller nanopores were involved in the liquid infiltration. Eventually, as the liquid infiltration volume reached the nanopore volume, the system became nearly incompressible. The Instron machine measured continuously the piston pressure and the piston displacement (d_p).

The liquid infiltration volume can be assessed as $d_p A_p$. The nominal flux in a nanopore with a radius of R can be estimated as $Q = v_p A_p / N_p$, where N_p is the nanopore number density. The value of N_p can be obtained through $f V_{pore}/(\pi R^2 \xi)$, where V_{pore} is the specific nanopore volume, ξ is the effective liquid infiltration depth, and f is the BET analysis result of the probability density of pore volume distribution. According to the equation $\tilde{\eta} = \tau R/(4\bar{v})$, the nominal viscosity can be estimated as $\tilde{\eta} = \pi P R^4/(8QL)$, where L is assumed half of the nanoporous particle size. P is the pressure acting on the infiltrating water liquid phase and can be measured from the sorption isotherm curve at corresponding temperature and loading rate following the analysis procedure discussed in Refs. 11 and 52. The calculated results are plotted in Figure 7. It is seen that the nominal viscosity decreases with the increase of temperature. Besides, the smaller nanopore radius is, the lower viscosity is, which agrees qualitatively with the results of NEMD simulations (despite the different working conditions in experiment and simulation).

Note that there are several factors making it prohibitively difficult for quantitative matching between simulation and experiment: (1) the nanoporous carbon used in experiment has some variations in its pore size; (2) the pore network in nanoporous carbon is quite complicated; (3) the porous carbon surface is modified by silyl groups, which makes it difficult to analyze or reproduce the exact surface structure in simulation; and (4) the loading rate in experiment cannot be very high yet the simulation in MD cannot be very slow. The MD simulation in the present paper is focused on an "idealized" nanofluidic model so as to reveal some intrinsic trends and molecular mechanisms. Nevertheless, the qualitative matching trends shown in Figures 2 (simulation) and 7 (experiment) have demonstrated the feasibility of the current numerical approach and experimental setup in the present preliminary study. We envision that the qualitative trends reported in this paper are applicable to all nanoporous materials. More quantitative coordination between simulation and experiment will be reported in the future, including the effect of surface group in experiment and modeling more complicated surface functional group structure.

CONCLUDING REMARKS

The temperature-dependent transport behaviors of water molecules inside CNTs are studied by using non-equilibrium molecular dynamics simulations. Both the effective shear stress and nominal viscosity decrease with the increase of temperature, owing to the relatively less severe confinement effect. The thermal effect is coupled with the tube size and transport rate effects, where in smaller tubes or at higher flow rates, the transport resistance is more temperature sensitive.

Moreover, with the addition of ions, the shear stress of electrolyte transport is higher (compare with that of pure water) owing to the more prominent liquid-solid wall interaction. The findings are qualitatively verified by a pressure-induced infiltration experiment on a nanoporous carbon/water system.

The thermally dependent nanofluidic transport behaviors may provide insights for designing temperature controlled nanodevices. For example, a low transport resistance can be beneficial for nanoconductors, whereas a high shear stress can be employed for high-performance energy dissipation nanomaterials,[53] whose energy density can be controlled through temperature. Besides, the system performance can be further optimized by take into account the pore size effect, transport rate effect, variation of the liquid phase, or surface modification. Since the transport behavior changes when ions are added to the liquid phase, the study may also shed some light on separating molecules or ions.

ACKNOWLEDGMENTS

The work was supported by the World Class University program through the National Research Foundation of Korea (Grant No. R32-2008-000-20042-0). Xi Chen acknowledges supports from Changjiang Scholar Program from the Ministry of Education of China, Defense Advanced Research Projects Agency (Grant No. W91CRB-11-C-0112), National Science Foundation (Grant No. CMMI-0643726), National Natural Science Foundation of China (Grant No. 11172231), and International Joint Research Project sponsored by Tsinghua University (Grant No. 20121080050).

[1] R. Helmy, Y. Kazakevich, C. Ni, and A. Y. Fadeev, J. Am. Chem. Soc. **127**, 12446–12447 (2005).
[2] W. Sparreboom, A. Vandenberg, and J. C. T. Eijkel, Nat. Nanotechnol. **4**, 713–720 (2009).
[3] L. Bocquet and E. Charlaix, Chem. Soc. Rev. **39**, 1073–1095 (2010).
[4] R. B. Schoch, J. Han, and P. Renaud, Rev. Modern Phys. **80**, 839–883 (2008).
[5] J. K. Holt, Adv. Mater. **21**, 3542–3550 (2009).
[6] K. Shirono, N. Tatsumi, and H. Daiguji, J. Phys. Chem. B **113**, 1041–1047 (2009).
[7] H. Daiguji, Chem. Soc. Rev. **39**, 901–911 (2010).
[8] G. Hummer, J. G. Rasalah, and J. P. Noworyta, Nature (London) **414**, 188–190 (2001).
[9] M. Majumder, N. Chopra, R. Andrews, and B. J. Hinds, Nature (London) **438**, 44 (2005).
[10] J. K. Holt, H. G. Park, Y. M. Wang, M. Stadermann, A. B. Artyukhin, C. P. Grigoropoulos, A. Noy, and O. Bakajin, Science **312**, 1034–1037 (2006).
[11] X. Chen, G. Cao, A. Han, V. K. Punyamurtula, L. Liu, P. J. Culligan, T. Kim, and Y. Qiao, Nano Lett. **8**, 2988–2992 (2008).
[12] V. P. Sokhan, D. Nicholson, and N. Quirke, J. Chem. Phys. **117**, 8531 (2002).
[13] C. Cottin-Bizonne, B. Cross, A. Steinberger, and E. Charlaix, Phys. Rev. Lett. **94**, 056102 (2005).
[14] B. Xu, Y. Li, T. Park, and X. Chen, J. Chem. Phys. **135**(14), 144703 (2011).
[15] S. Joseph and N. R. Aluru, Nano Lett. **2**, 452–458 (2008).
[16] A. V. Raghunathan and N. R. Aluru, Phys. Rev. E **76**, 011202 (2007).
[17] Y. He, D. Gillespie, D. Boda, I. Vlassiouk, R. Eisenberg, and Z. Siwy, J. Am. Chem. Soc. **131**, 5194–5202 (2009).
[18] B. Xu, Y. Qiao, Y. Li, Q. Zhou, and X. Chen, Appl. Phys. Lett. **98**, 221909 (2011).
[19] U. Vermesh, J. W. Choi, O. Vermesh, R. Fan, J. Nagarah, and J. R. Heath, Nano Lett. **9**, 1315–1319 (2009).
[20] J. Zhao, P. J. Culligan, Y. Qiao, Q. Zhou, Y. Li, M. Tak, T. Park, and X. Chen, J. Phys.: Condens. Matter **22**, 315301 (2010).
[21] H. Gu, J. D. Marth, P. C. Orban, H. Mossmann, and K. Rajewsky, Science **265**, 100–103 (1994).
[22] P. M. Kampmeyer, J. Appl. Phys. **23**, 99–102 (1952).
[23] S. Vaitheeswaran, J. C. Rasaiah, and G. Hummer, J. Chem. Phys. **121**, 7955–7965 (2004).
[24] M. J. Longhurst and N. Quirke, Nano Lett. **7**, 3324–3328 (2007).
[25] C. Liu and Z. Li, Phys. Rev. Lett. **105**, 174501 (2010).
[26] A. Han and Y. Qiao, Appl. Phys. Lett. **91**, 173123 (2007).
[27] P. Koumoutsakos, Annu. Rev. Fluid Mech. **37**, 457–487 (2005).
[28] K. P. Travis and K. E. Gubbins, J. Chem. Phys. **112**, 1984–1994 (2000).
[29] S. Plimpton, J. Comput. Phys. **117**, 1–19 (1995).
[30] J. Zhao, L. Liu, P. J. Culligan, and X. Chen, Phys. Rev. E **80**, 061206 (2009).
[31] H. J. C. Berendsen, J. R. Grigera, and T. P. Straatsma, J. Phys. Chem. **24**, 6269–6271 (1987).
[32] S. Chowdhuri and A. Chandra, J. Chem. Phys. **115**, 3732–3741 (2001).
[33] S. Koneshan, J. C. Rasaiah, R. M. Lynden-Bell, and S. J. Lee, J. Phys. Chem. B **102**, 4193–4204 (1998).
[34] T. Werder, J. H. Walther, R. L. Jaffe, T. Halicioglu, and P. Koumoutsakos, J. Phys. Chem. B **107**, 1345–1352 (2003).
[35] T. A. Andrea, W. C. Swope, and H. C. Andersen, J. Chem. Phys. **79**, 4576–4584 (1984).
[36] R. W. Hockney and J. W. Eastwood, *Computer Simulation Using Particles* (Taylor & Francis, New York, 1989).
[37] J. C. Rasaiah, J. P. Noworyta, and S. Koneshan, J. Am. Chem. Soc. **122**, 11182–11193 (2000).
[38] C. Vega and E. d. Miguel, J. Chem. Phys. **126**, 154707 (2007).
[39] K. Koga, G. T. Gao, H. Tanaka, and X. C. Zeng, Nature (London) **412**, 802–805 (2001).
[40] D. Takaiwa, I. Hatano, K. Koga, and H. Tanaka, Proc. Natl. Acad. Sci. U.S.A. **105**, 39–43 (2008).
[41] J. Koplik, J. R. Banavar, and J. F. Willemsen, Phys. Rev. Lett. **60**, 1282–1285 (1988).
[42] G. S. Heffelfinger and F. van Swol, J. Chem. Phys. **100**, 7548 (1994).
[43] I. Hanasaki and A. Nakatani, J. Chem. Phys. **124**, 144708 (2006).
[44] J. A. Thomas and A. J. H. McGaughey, Nano Lett. **8**, 2788–2793 (2008).
[45] T. Kim, W. Lu, H. Lim, A. Han, and Y. Qiao, Appl. Phys. Lett. **98**, 053106 (2011).
[46] W. Sparreboom, A. Berg, and J. C. T. Eijkel, New J. Phys. **12**, 015004 (2010).
[47] J. A. Thomas and A. J. H. McGaughey, J. Chem. Phys. **128**, 084715 (2008).
[48] A. Luzar and D. Chandler, Nature (London) **379**, 55–57 (1996).
[49] T. Werder, J. H. Walther, R. L. Jaffe, T. Halicioglu, F. Noca, and P. Koumoutsakos, Nano Lett. **1**, 697–702 (2001).
[50] A. Kalra, S. Garde, and G. Hummer, Proc. Natl. Acad. Sci. U.S.A. **100** 10175–10180 (2003).
[51] A. Plecis, R. B. Schoch, and P. Renaud, Nano Lett. **5**, 1147–1155 (2005).
[52] A. Han, W. Lu, V. Punyamurtula, X. Chen, F. Surani, T. Kim, and Y. Qiao, J. Appl. Phys. **104**, 124908 (2008).
[53] X. Chen, F. B. Surani, X. Kong, V. K. Punyamurtula, and Y. Qiao, Appl. Phys. Lett. **89**, 241918 (2006).